10.2352/EI.2022.34.15.COLOR-159

Improvements to Color Image and Machine Learning Based Thin-film Nitrate Sensor Performance Prediction: New Texture Features, Repeated Cross-validation, and Auto-tuning of Hyper-parameters[1]

Xihui Wang, Ye Mi, Ali Shakouri, George T.C. Chiu, Jan P. Allebach;
Purdue University, West Lafayette, Indiana, United States

Abstract

A correlation between thin-film nitrate sensor performance and sensor surface texture was hypothesized. Based on this hypothesis, we began research on the application of machine learning methods on thin-film nitrate sensor surface images to predict its performance. This technology would enable real-time optimization adjustments to be made during production to greatly increase the quality of the sensors while reducing costs associated with testing and defective sensors. Recently, we have made progress in the addition of new texture features, repeated cross-validation methods, and auto-tuning of hyperparameters.

Introduction

We intend to build a roll-to-roll (R2R) sensor manufacturing line in order to fabricate low-cost thin-film nitrate sensors in high volume. Those thin-film nitrate sensors are designed to monitor soil conditions in the field. The study of nitrate sensors indicates that the performance of the sensors can be affected by the non-uniform coating of the ion-selective membrane (ISM) [1], [2]. In order to make rapid adjustments during the fabrication process, image-based machine learning techniques are used to predict the manufactured sensor performance.

The current process shown in Figure 1 is to use the R2R manufacturing system to print the nitrate sensors in batches. The manufactured sensors are taken for imaging, and then taken to a dedicated laboratory for measurement. At the moment, testing is done in labs. A fitted curve is derived from the physics hypothesis and the measured performance signal after smoothing to reduce the noise. The predicted performance is compared against the fitted performance curve.

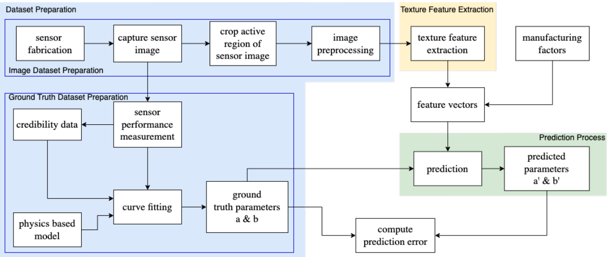
Dataset Preparation
Texture Feature Extraction
sensor fabrication
capture sensor image
crop active region of sensor image
image preprocessing
texture feature extraction
manufacturing factors
Image Dataset Preparation
Ground Truth Dataset Preparation
feature vectors
credibility data
sensor performance measurement
Prediction Process
prediction
predicted parameters a' & b'
curve fitting
ground truth parameters a & b
physics based model
compute prediction error

Figure 1. *Overview of Prediction System for Training and Inferencing.*

This paper is a continuation of the previous work [3], [4]. We will examine several ways to extract features from captured sensor images (yellow region shown in Figure 1) and a modified version of the auto-tuned prediction system (green region shown in Figure 1) in this paper. With the goal of fully automating the process, this prediction system is based on different machine-learning techniques and cross-validation methods. Performance is improved by auto-tuning the hyperparameter settings for the machine learning models.

Dataset Preparation

As part of this project, both sensor image data and ground truth parameters data are generated by ourselves.

Image Data Preparation

According to the physics hypothesis [2], the sensor active region marked in Figure 2(b) is related to the sensor performance. In order to capture the sensor active region image, a silicon wafer is placed underneath the nitrate sensor and an Electro-Optical System (EOS)[2] camera attached to a microscope is used. The sensor imaging setup is shown in Figure 2(a) and Figure 2(c) is an example of the captured non-contact sensor image.

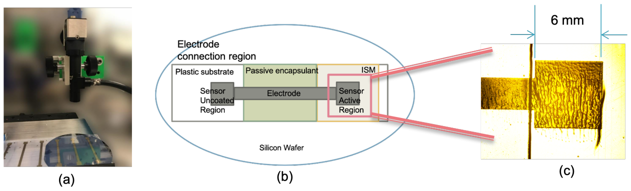

Figure 2. *(a) Experiment Setup for Capturing Sensor Images;*
(b) Structure of the Nitrate Sensor;
(c) Example of Captured Sensor Active Region Image.

Following is the procedure that is shown in the system pipeline in Figure 1: once the sensor images have been captured, we use the method described in the previous paper [3] to segment the active sensor region from the captured image.

As soon as the sensor active region is cropped from the original non-contact sensor image, we apply the image preprocessing techniques discussed in [3] to enhance texture details in the sensor active region image. An example of this procedure is given in Figure 3.

[1] Research supported by the SMART films consortium (https://www.purdue.edu/discoverypark/birck/research/smart-films.php).

[2] Electro-Optical System Inc, Phoenixville, PA 19460.

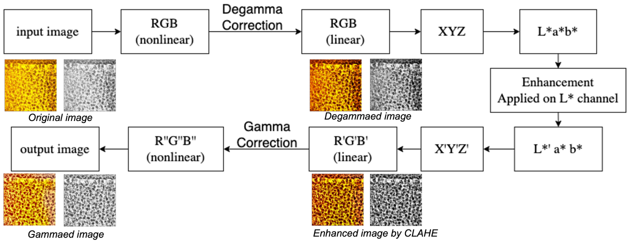

Figure 3. *Image Data Preprocessing Procedure.*

Sensor Performance Data Preparation

The sensor response signals in this experiment are degraded by human error during the measurement of sensor performance rather than sensor defects. Therefore, the outliers should be eliminated before generating the ground truth parameters using the method described in [4].

The physics-based model [2] suggests that the change of potential voltage over time is a logarithmic growth curve. Hence, Equation 1 is used here to generate the ground truth parameters a and b for the inlier performance signals.

$$V_{fit}(t) = a \cdot log(t) + b \tag{1}$$

Figure 4 illustrates the modified curve fitting method proposed in [4]. The weighted Levenberg-Marquardt algorithm [7] is used to find the ground truth parameters that give the best fitting curve V_{fit}, while the weighting factor is dependent upon the dynamic credibility data.

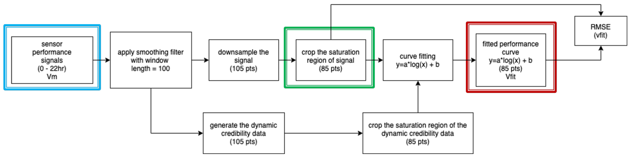
sensor performance signals (0 - 22hr) Vm
apply smoothing filter with window length = 100
downsample the signal (105 pts)
crop the saturation region of signal (85 pts)
curve fitting y=a*log(x) + b
fitted performance curve y=a*log(x) + b (85 pts) Vfit
RMSE (vfit)
generate the dynamic credibility data (105 pts)
crop the saturation region of the dynamic credibility data (85 pts)

Figure 4. *Ground Truth Data Preparation Procedure Applied to the Inlier Sensor Data after Outlier Exclusion Based on the Credibility Analysis.*

We use the weighted root-mean-square error (RMSE) denoted as $RMSE_{CF}$ to evaluate the accuracy of the fitted curve. CF stands for curve fitting process, and N is the total number of time points. The weights $c(x)$ are the inversely proportional to the dynamic credibility data.

$$RMSE_{CF}(mV) = \sqrt{\frac{1}{N}\sum_{x} c(x)\left(V_{fit}(x) - V_d(x)\right)^2} \tag{2}$$

Figure 5(a) illustrates the difference between the original measured sensor performance signal V_m, the down-sampled and smoothed signal V_d, and the fitted curve V_{fit} in the saturated region. The $RMSE_{Vm}$ is the weighted RMSE calculated between V_{fit} and the down-sampled V_m while the $RMSE_{Vs}$ is the weighted RMSE calculated between V_{fit} and the down-sampled smoothed V_s. Figure 5(b) shows the dynamic credibility data for the corresponding sensor.

Texture Feature Extraction

Gray-level Co-occurrence Matrix (GLCM)

The GLCM method [8] is a commonly used image descriptor representing the distance and angular spatial relationships over an image sub-region of a specific size.

The gray-scale sensor image contains 255 gray levels, making the size of our GLCM matrix 255 × 255 (denoted as $P_u(i,j)$). It is unreasonable to use the entire GLCM matrix as the texture feature. Hence, we calculated the GLCM features [8] from the normalized GLCM matrix $P(i,j) = P_u(i,j)/R$, where R is the total number of pixel pairs. Figure 6 shows the GLCM features that we explored. The features marked in blue are the most commonly used, and the equations marked in green are the parameters that are used to calculate the remaining GLCM features.

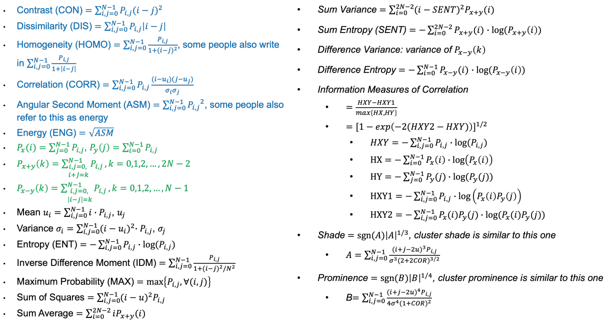

- Contrast (CON) = $\sum_{i,j=0}^{N-1} P_{i,j}(i-j)^2$
- Dissimilarity (DIS) = $\sum_{i,j=0}^{N-1} P_{i,j}|i-j|$
- Homogeneity (HOMO) = $\sum_{i,j=0}^{N-1} \frac{P_{i,j}}{1+(i-j)^2}$, some people also write in $\sum_{i,j=0}^{N-1} \frac{P_{i,j}}{1+|i-j|}$
- Correlation (CORR) = $\sum_{i,j=0}^{N-1} P_{i,j} \frac{(i-u_i)(j-u_j)}{\sigma_i\sigma_j}$
- Angular Second Moment (ASM) = $\sum_{i,j=0}^{N-1} {P_{i,j}}^2$, some people also refer to this as energy
- Energy (ENG) = $\sqrt{ASM}$
- $P_x(i) = \sum_{j=0}^{N-1} P_{i,j}$, $P_y(j) = \sum_{i=0}^{N-1} P_{i,j}$
- $P_{x+y}(k) = \sum_{\substack{i,j=0,\\ i+j=k}}^{N-1} P_{i,j}\,, k = 0,1,2,\dots,2N-2$
- $P_{x-y}(k) = \sum_{\substack{i,j=0,\\ |i-j|=k}}^{N-1} P_{i,j}\,, k = 0,1,2,\dots,N-1$
- Mean $u_i = \sum_{i,j=0}^{N-1} i \cdot P_{i,j}$, u_j
- Variance $\sigma_i = \sum_{i,j=0}^{N-1} (i-u_i)^2 \cdot P_{i,j}$, σ_j
- Entropy (ENT) = $-\sum_{i,j=0}^{N-1} P_{i,j} \cdot \log(P_{i,j})$
- Inverse Difference Moment (IDM) = $\sum_{i,j=0}^{N-1} \frac{P_{i,j}}{1+(i-j)^2/N^2}$
- Maximum Probability (MAX) = $\max\{P_{i,j}, \forall(i,j)\}$
- Sum of Squares = $\sum_{i,j=0}^{N-1} (i-u)^2 P_{i,j}$
- Sum Average = $\sum_{i=0}^{2N-2} iP_{x+y}(i)$
- *Sum Variance* = $\sum_{i=0}^{2N-2} (i-SENT)^2 P_{x+y}(i)$
- *Sum Entropy (SENT)* = $-\sum_{i=0}^{2N-2} P_{x+y}(i) \cdot \log(P_{x+y}(i))$
- *Difference Variance: variance of* $P_{x-y}(k)$
- *Difference Entropy* = $-\sum_{i=0}^{N-1} P_{x-y}(i) \cdot \log(P_{x-y}(i))$
- *Information Measures of Correlation*
  - $= \frac{HXY-HXY1}{max\{HX,HY\}}$
  - $= [1 - exp(-2(HXY2 - HXY))]^{1/2}$
    - $HXY = -\sum_{i,j=0}^{N-1} P_{i,j} \cdot \log(P_{i,j})$
    - $\mathrm{HX} = -\sum_{i=0}^{N-1} P_x(i) \cdot \log(P_x(i))$
    - $\mathrm{HY} = -\sum_{j=0}^{N-1} P_y(j) \cdot \log(P_y(j))$
    - $\mathrm{HXY1} = -\sum_{i,j=0}^{N-1} P_{i,j} \cdot \log\left(P_x(i)P_y(j)\right)$
    - $\mathrm{HXY2} = -\sum_{i,j=0}^{N-1} P_x(i)P_y(j) \cdot \log(P_x(i)P_y(j))$
- *Shade* = $\mathrm{sgn}(A)|A|^{1/3}$, *cluster shade is similar to this one*
  - $A = \sum_{i,j=0}^{N-1} \frac{(i+j-2u)^3 P_{i,j}}{\sigma^3(2+2COR)^{3/2}}$
- *Prominence* = $\mathrm{sgn}(B)|B|^{1/4}$, *cluster prominence is similar to this one*
  - $B = \sum_{i,j=0}^{N-1} \frac{(i+j-2u)^4 P_{i,j}}{4\sigma^4(1+COR)^2}$

Figure 6. *GLCM Features.*

Sequential Forward Floating Selection (SFFS)

To avoid having less meaningful features disturb the prediction model, we applied the sequential forward floating selection (SFFS) method [9], [10] to select a subset of GLCM features to minimize the prediction error. Figure 7 shows the SFFS procedure and the size of subset changes during each iteration [10].

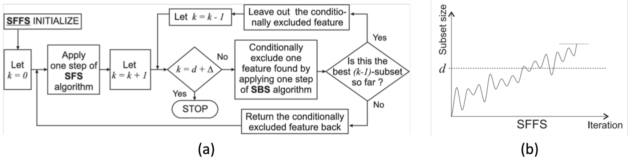
SFFS INITIALIZE
Let $k = 0$
Apply one step of SFS algorithm
Let $k = k + 1$
$k = d + \Delta$
No
Yes
STOP
Let $k = k - 1$
Leave out the conditionally excluded feature
Conditionally exclude one feature found by applying one step of SBS algorithm
Is this the best (k-1)-subset so far ?
Yes
No
Return the conditionally excluded feature back
(a)
Subset size
d
SFFS
Iteration
(b)

Figure 7. *(a) SFFS Procedure;*
(b) Example of the Subset Size Changes During the SFFS Procedure.

Figure 8(a) and (b) gives an example of the SFFS method applied to the ground truth parameters a and b. The total number of GLCM features is 27; and we are using the 5-fold cross-validation method to evaluate the performance during subset selection. The blue dots represent the average performance at each desired num-

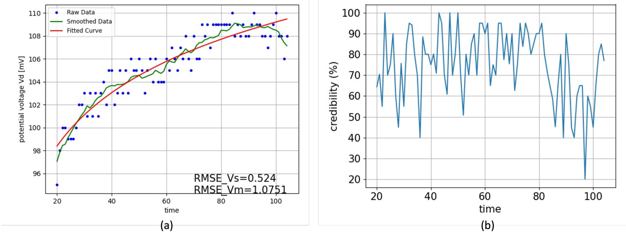

Figure 5. *(a) Example of Fitted Logarithmic Curve;*
(b) Dynamic Credibility Data.

ber of output subset size, and the light blue region represents the variance of the performance. The performance for the regression model is the negative root mean square error calculated between the ground truth parameter and the predicted parameter. *gt* stands for the ground truth value while *pred* stands for the predicted value.

$$RMSE_{SFFS\_a}(mV) = \sqrt{\frac{1}{N}\sum_{x}\left(a_{pred}(x) - a_{gt}(x)\right)^2} \qquad (3)$$

$$RMSE_{SFFS\_b}(mV) = \sqrt{\frac{1}{N}\sum_{x}\left(b_{pred}(x) - b_{gt}(x)\right)^2} \qquad (4)$$

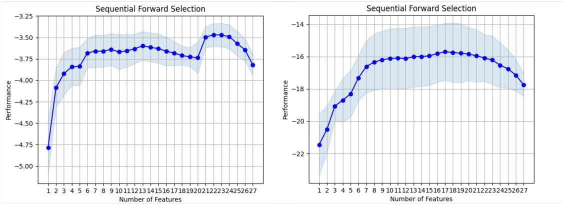

Figure 8. *(a) SFFS Subset of Parameter a;*
(b) SFFS Subset of Parameter b.

In this case, we choose the nine features that have been selected by the SFFS method for both ground truth parameters a and b.

Angularly Averaged Power Spectrum (AAPS)

In order to calculate the angularly averaged spectrum signal [11], we apply the 2D Fourier transform to the grayscale sensor image to obtain the 2D power spectrum density (PSD) signal first.

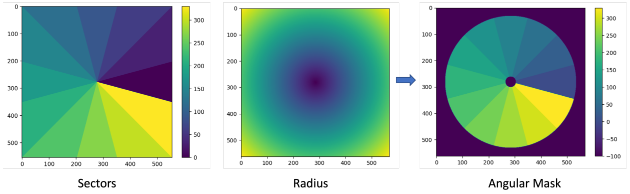

Figure 9. *Angular Mask Generation.*

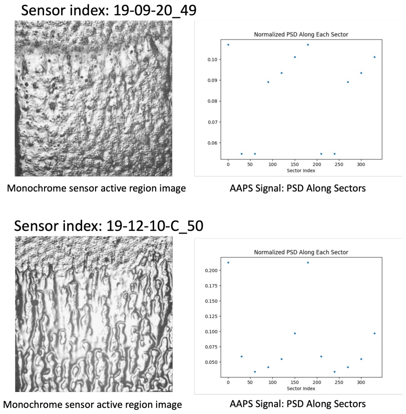

Figure 10. *Example of AAPS Results.*

Afterwards, we set the angular interval $\Delta\theta$ in degrees, determine which angular interval the pixel belongs to and generate the sector mask. Meanwhile, we could calculate the distance from the center frequency to each frequency (radius) and create the radius mask. To remove spectral artifacts at both low and high frequencies, we set up a radius limitation by defining the r_{Min} and r_{Max} parameters to exclude PSD values at frequencies outside this range. As a result, we can generate the angular mask by combining the sector mask, the radius mask, and the limit parameters. Figure 9 demonstrates an example of generating the angular mask with $\Delta\theta$ equal to 30 degrees, r_{Min} equals 0.0391 cycles/pixel or 20 pixels for a 512×512 pixel DFT, and r_{Max} equals 0.488 cycles/pixel or 250 pixels for a 512×512 pixel DFT.

By normalizing the total PSD along with each sector by the total energy contained in each sector, we get the AAPS signal demonstrated in Figure 10. As shown in the figure, the AAPS signal varys a lot given different sensor active region images.

Radially Averaged Power Spectrum (RAPS)

To calculate the radially averaged power spectrum (RAPS) [12] signal of each sensor image, we need to convert the image from gray level (reflectance) I_r to absorptance I_a by $I_a = 1 - I_r/255$. Then similar to the AAPS feature, we apply the 2D Fourier transform to the absorptance image I_a and get the 2D PSD signal.

We then set up the ring width r_w, calculate the radius at each pixel location, and generate the circular ring mask as the RAPS radial mask, as shown in Figure 11.

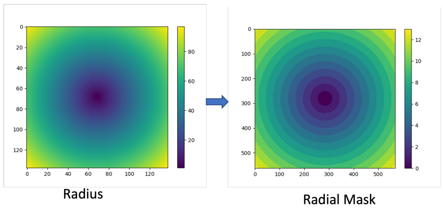

Figure 11. *Radial Mask Generation.*

The RAPS signal is computed by normalizing the total PSD in each circular ring by the total energy of the image contained within the circular rings. Energy is largely concentrated in the center. Changing the ring width r_w would result in different RAPS results, as shown in Figure 12. The sensor active region image used for this example is the sensor index 19-12-10-C_50 shown in Figure 10.

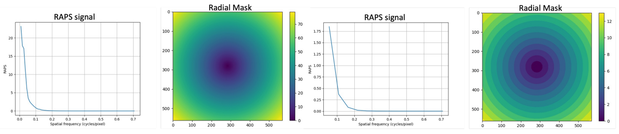

Ring width = 0.00977 cycles/pixel
or 5 pixels for a 512 x 512 DFT
# of rings = 79

Ring width = 0.0586 cycles/pixel
or 30 pixels for a 512 x 512 DFT
# of rings = 13

Figure 12. *Example of RAPS Results.*

Prediction System

Following the previous work, the support vector regression (SVR) model [17] and the alpha-trimmed mean random forest (ATRF) model [4] are selected as the prediction models.

ATRF involves applying the alpha-trimmed mean filter [20] to all the predicted values from each decision tree in the random forest [19], and obtaining the predicted value of the ATRF.

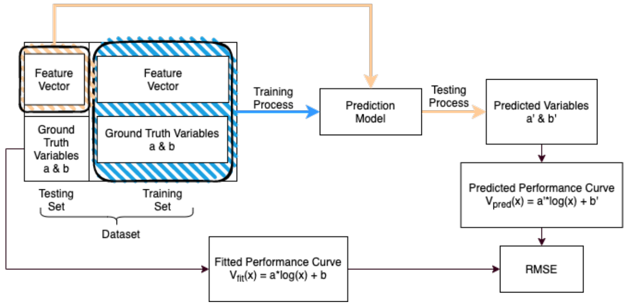
Feature Vector
Ground Truth Variables a & b
Feature Vector
Ground Truth Variables a & b
Testing Set
Training Set
Dataset
Training Process
Prediction Model
Testing Process
Predicted Variables a' & b'
Predicted Performance Curve $V_{pred}(x) = a'*log(x) + b'$
Fitted Performance Curve $V_{fit}(x) = a*log(x) + b$
RMSE

Figure 13. Structure of The Prediction Model.

The structure of the prediction system is shown in Figure 13. The system takes the generated ground truth parameters and the feature vectors (texture features combined with manufacturing factors) as input during the training process. To test the accuracy of the prediction model, the system uses the feature vector as input, and outputs the predicted performance parameters during the testing process.

Data normalization is necessary when the features are in different ranges, and we use the Min-max normalization method (MMNM) [13] to normalize each feature to the range [0, 1].

To evaluate the performance of the prediction system, $RMSE_{pred}$ is calculated between the predicted curve based on the predicted parameters a' and b', and the fitted curve generated based on the ground truth parameters a and b.

$$V_{fit}(x) = a \cdot log(x) + b \tag{5}$$

$$V_{pred}(x) = a' \cdot log(x) + b' \tag{6}$$

$$RSME_{pred} = \sqrt{\frac{1}{N}\sum_{x}(V_{pred}(x) - V_{fit}(x))^2} \tag{7}$$

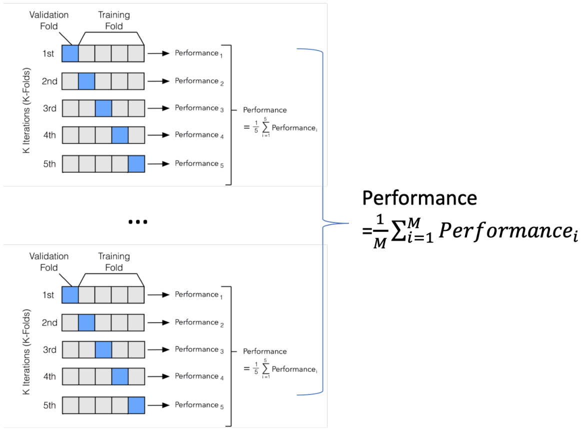

Figure 14. Structure of Repeated K-fold Cross-validation Method.

A single k-fold cross-validation run will result in a noisy estimate of model performance, because different folding sets will result in various prediction performances, especially for a small dataset. Due to the limitation of the size of our dataset, we choose the repeated cross-validation (RCV) method [14] to estimate the accuracy of our prediction model. The RCV is performed by randomly folding the entire dataset and repeating the traditional k-fold cross-validation (CV) procedure multiple times. Each cross-validation procedure is performed with a different random folding of the dataset. The prediction performance will be the average prediction performance of each k-fold CV as shown in Figure 14.

Auto-tuning Procedure

Hyperparameters are the specified parameters set before training the prediction model and could affect the models' accuracy. We use the nested cross-validation (NCV) method [15], the grid search method, and the random search method [16] to find the optimized hyperparameter setting with the best prediction performance. This process, referred to as auto-tuning, is shown in Figure 15.

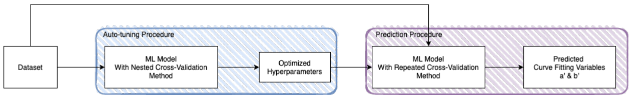
Dataset
Auto-tuning Procedure
ML Model With Nested Cross-Validation Method
Optimized Hyperparameters
Prediction Procedure
ML Model With Repeated Cross-Validation Method
Predicted Curve Fitting Variables a' & b'

Figure 15. Overview of The Auto-tuning Prediction System.

As part of the auto-tuning process, two search methods are considered to find the optimal combination for constructing the prediction model: the grid search method, which is the exhaustive search way, and the random search, which uses random combinations of hyperparameters. In our case, we use the grid search method for the ATRF model, and the random search method for the SVR model.

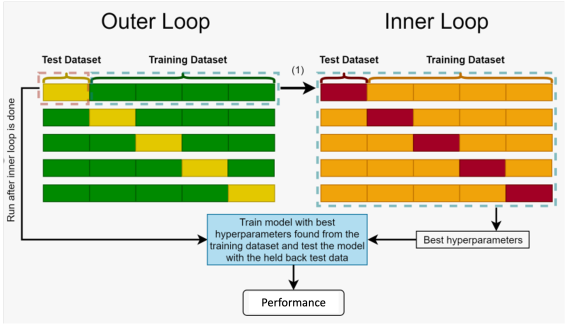
Outer Loop
Inner Loop
Test Dataset
Training Dataset
Test Dataset
Training Dataset
(1)
Run after inner loop is done
Train model with best hyperparameters found from the training dataset and test the model with the held back test data
Best hyperparameters
Performance

Figure 16. Structure of Nested Cross-validation Method.

The NCV method is developed by constructing a k-fold CV (inner loop) nested inside a k-fold CV (outer loop) as shown in Figure 16. The inner loop applies k-fold CV on the training dataset of the outer loop. The idea of the NCV method is to search for the optimized hyperparameters in the inner loop and to evaluate the optimized hyperparameters setting in the outer loop for comparison and selection. We repeat the NCV for 50 trials, and the optimal setting is the one that exhibits the highest frequency of results.

Experiment Results

With the use of nested cross-validation and two search methods, we designed an auto-tuning prediction system for higher performance accuracy. The nested cross-validation method runs fifty trials with five folds in the outer loop, and three folds in the inner loop. There are three hyperparameters for the SVR model: the decision boundary ε in the range [1e-6, 1], the regularization parameter C in the range [10, 1e6], and the RBF kernel [18] parameter γ in the range [1e-6, 1]. For the ATRF model, there is only one hyperparameter, which is the number of decision trees n_{tree} in the range [1k, 10k] contained in the forest. There was no limit specified for the depth of each decision tree, so all nodes were expanded until all leaves were pure. The optimized combination of hyperparameters is then used to construct the prediction model.

To obtain a reliable and stable estimate of system performance, we run 200 trials of the repeated 5-fold cross validation procedure to train and evaluate our system. It is the equivalent of running a single test for 1000 times.

The feature vectors with which we have experimented are shown in Table 1. In addition to texture features, the manufacturing factors (MF) are added to the feature vector as input to the prediction system. The manufacturing factors include the average measured sensor thickness, and three process control parameters: solid content, line speed, and flow rate. Each manufacturing factor is a floating-point number. All features within each method will be normalized to the range [0, 1] before feeding them to the prediction model.

Feature Vectors Implemented in the Image-based Prediction System

Method	Feature Vector
M1	LBP (uniform) + MF
M2	LBP (nri_uniform) + MF
M3	GP + LBP (uniform) + MF
M4	GP + LBP (nri_uniform) + MF
M5	GLCM (5 features) + MF
M6	GLCM (9 features by SFFS) + MF
M7	GLCM (27 features) + MF
M8	AAPS + MF
M9	RAPS (spatial frequency 0-0.09 cycles/pixel) + MF
M10	RAPS (spatial frequency 0-0.18 cycles/pixel) + MF
M11	RAPS (spatial frequency 0-0.36 cycles/pixel) + MF

Methods 1 to 4 are discussed in [3]. The local binary pattern (LBP) features [5] are calculated with $P = 8$ pixels and $R = 3$ pixels mentioned in [3]. The Gaussian pyramid (GP) [6] contains three layers. Hence, applying the LBP method on each GP layer generates a 1D feature array three times longer.

Methods 5 to 7 are related to the 27 GLCM features. The GLCM matrix is calculated with a distance of 5 pixels and a 45 degree angle. The five features used in M5 are contrast, dissimilarity, homogeneity, correlation, and angular second moment. The nine features based on the SVR model selected by the SFFS method for Method 6 are dissimilarity, homogeneity, mean u_i and u_j, variance σ_i and σ_j, sum of squares, sum entropy, and information measures of correlation H_y.

The AAPS method is set with $\Delta\theta$ = 30 degree, r_{Min} = 0.0391 cycles/pixel, and r_{Max} = 0.488 cycles/pixel. The RAPS method is set with r_w = 5 pixels or 0.00977 cycles/pixel for a 512 × 512 pixel DFT for Methods 9 to 11.

The average RMSE and the standard deviation of RMSE are used to estimate the performance of the image-based prediction system.

$$RMSE_{pred}(mV) = \sqrt{\frac{1}{N}\sum_{x}\left(V_{fit}(x) - V_{pred}(x)\right)^2} \qquad (8)$$

As mentioned previously, the prediction result for each method is estimated by repeated 5-fold cross-validation with 200 trials.

The accuracy and the robustness of the image-based prediction system can be described by the average RMSE and the standard deviation shown in Table 2 for the SVR model and in Table 3 for the ATRF model. The dataset used in this experiment contains 108 sensors. The $StDev_{fold}$ represents the standard deviation over the performance for each fold within each trial while the $StDev_{trial}$ represents the standard deviation over the average performance for each trial.

Prediction Results for SVR Model

Method	$RMSE$ (mV)	$StDev_{fold}$ (mV)	$StDev_{trial}$ (mV)
M1	5.9094	1.1194	0.2152
M2	6.7825	1.3033	0.3433
M3	6.2308	1.1690	0.2545
M4	6.5245	1.0633	0.2692
M5	5.9377	1.1092	0.1574
M6	6.0645	1.0772	0.2005
M7	6.0743	1.1759	0.1986
M8	5.8192	1.1061	0.1589
M9	**5.7532**	**1.0620**	**0.1651**
M10	5.8111	1.0144	0.1581
M11	5.9991	1.0085	0.1740

Prediction Results for ATRF Model

Method	$RMSE$ (mV)	$StDev_{fold}$ (mV)	$StDev_{trial}$ (mV)
M1	**6.0726**	**1.0214**	**0.2503**
M2	6.1380	1.0258	0.2941
M3	6.1213	1.0362	0.2618
M4	6.5588	1.1077	0.2455
M5	7.3711	1.1717	0.3156
M6	6.7581	1.1483	0.3175
M7	6.8488	1.2270	0.3354
M8	6.8914	1.1841	0.2620
M9	6.3647	1.0660	0.2831
M10	6.4668	1.1021	0.2701
M11	6.4084	1.1229	0.2603

Conclusion

An image-based prediction system has been developed to accurately predict the potentiometric response of the nitrate sensor based on the preprocessed sensor active region images. This system allows us to monitor the sensors quality during the fabrication process with an R2R system in the future. This paper focuses primarily on the modifications we made to the texture extraction and the prediction system sections.

For the texture feature extraction section, we analyzed the GLCM descriptor, the AAPS features, and the RAPS features. To select a meaningful subset of features out of all features, we also applied the SFFS method.

For the prediction section, we used the repeated cross-validation method while training to make the prediction results more stable and reliable. In order to make the whole process automatic, we developed an auto-tuning technique using the nested cross-validation method, the grid search method, and the random search method.

References

[1] J. Hu, A. Stein, and P. Bühlmann, "Rational design of all-solid-state ion-selective electrodes and reference electrodes," TrAC Trends in Analytical Chemistry, vol. 76, pp. 102–114, 2016.

[2] X. Jin, A. Saha, H. Jiang, M. R. Oduncu, Q. Yang, S. Sedaghat, D. K. Maize, J. P. Allebach, A. Shakouri, N. J. Glassmaker, et al., "Steady-state and transient performance of ion-sensitive electrodes suitable for wearable and implantable electro-chemical sensing," IEEE Transactions on Biomedical Engineering, vol. 69, no. 1, pp. 96-107, 2021.

[3] X. Wang, K. Maize, Y. Mi, A. Shakouri, G. T. Chiu, and J. P. Allebach, "Thin-film nitrate sensor performance prediction based on preprocessed sensor images," Electronic Imaging, 2021.

[4] X. Wang, R. Wu, A. Sara, Y. Mi, A. Shakouri, G. T. Chiu, and J. P. Allebach, "Thin-film nitrate sensor performance prediction based on image analysis and credibility data to enable a certify as built framework," Manufacturing Science and Engineering Conference, 2022.

[5] T. Ojala, M. Pietikainen, and D. Harwood, "A comparative study of texture measures with classification based on featured distributions," Pattern Recognition, vol. 29, no. 1, pp. 51-59, 1996.

[6] E. H. Adelson, C. H. Anderson, J. R. Bergen, P. J. Burt, J. M. Ogden, "Pyramid methods in image processing," RCA Engineer, vol. 29, no. 6, pp. 33-41, 1984.

[7] H. P. Gavin, "The Levenberg-Marquardt algorithm for nonlinear least squares curve-fitting problems," Department of Civil and Environmental Engineering, Duke University, 2019.

[8] R. M. Haralick, K. Shanmugam, and I. H. Dinstein, "Textural features for image classification," IEEE Transactions on Systems, Man, and Cybernetics, no. 6, pp. 610–621, 1973.

[9] P. Pudil, J. Novovicová, and J. Kittler, "Floating search methods in feature selection," Pattern Recognition Letters, vol. 15, no. 11, pp. 1119–1125, 1994.

[10] P. Somol, J. Novovicová, and P. Pudil, "Efficient feature subset selection and subset size optimization," Pattern Recognition Recent Advances, IntechOpen, 2010.

[11] J. S. Bendat and A. G. Piersol, Engineering Applications of Correlation and Spectral Analysis, John Wiley and Sons, New York, 1980.

[12] R. A. Ulichney, "Dithering with blue noise," Proceedings of the IEEE, vol. 76, no. 1, pp. 56–79, 1988.

[13] T. Jayalakshmi, and A. Santhakumaran, "Statistical normalization and back propagation for classification," International Journal of Computer Theory and Engineering, vol. 3, no. 1, pp. 1793-8201, 2011.

[14] P. Burman, "Estimation of optimal transformations using v-fold cross validation and repeated learning-testing methods," Sankhyā: The Indian Journal of Statistics, Series A, vol. 52, no. 3, pp. 314–345, 1990.

[15] M. Stone, "Cross-validatory choice and assessment of statistical predictions," Journal of the Royal Statistical Society: Series B (Methodological), vol. 36, no. 2, pp. 111–133, 1974

[16] M. Schumer and K. Steiglitz, "Adaptive step size random search," IEEE Transactions on Automatic Control, vol. 13, no. 3, pp. 270–276, 1968.

[17] A. J. Smola and B. Schölkopf, "A tutorial on support vector regression," Statistics and Computing, vol. 14, no. 3, pp. 199–222, 2004.

[18] M. T. Musavi, W. Ahmed, K. H. Chan, K. B. Faris, and D. M. Hummels, "On the training of radial basis function classifiers," Neural Networks, vol. 5, no. 4, pp. 595–603, 1992.

[19] G. Biau and E. Scornet, "A random forest guided tour," Test, vol. 25, no. 2, pp. 197–227, 2016.

[20] J. Bednar and T. Watt, "Alpha-trimmed means and their relationship to median filters," IEEE Transactions on Acoustics, Speech, and Signal Processing, vol. 32, no. 1, pp. 145–153, 1984.

Author Biography

Xihui Wang *received her B.S. (2016) and M.S. (2019) in Electrical Engineering from Purdue University and is currently a Ph.D. candidate in Purdue ECE. Her research focuses on image processing, computer vision, and machine learning.*

Ye Mi *received his Ph.D. in Nuclear Engineering from Purdue University in 1998. He received both his M.S. and B.S. from Tsinghua University in China, majoring in Nuclear Physics and Nuclear Instrumentation respectively. In recent years, he has been focusing on R&D of industrial processing tomography. Currently, he is working on inline metrology of R2R systems.*

Ali Shakouri *is an electrical and computer engineering professor and director of the Birck Nanotechnology Center at Purdue University. He received his Ph.D. from Caltech. His research focuses on quantum electronics, mutual interaction of heat, light, and electricity in nanomaterials and devices, lock-in imaging, and advanced image processing with applications to nanoscale thermal measurements and roll-to-roll process monitoring. He leads a team to manufacture low-cost smart internet of thing (IoT) devices and sensor network for applications in advanced manufacturing and agriculture.*

George T. C. Chiu *is a Professor with the School of Mechanical Engineering with courtesy appointments in the School of Electrical and Computer Engineering and the Department of Psychological Sciences at Purdue University. He worked on designing printers and multifunction devices with Hewlett-Packard, Palo Alto, CA, USA. From 2011 to 2014, he served as the Program Director for the Control Systems Program with the National Science Foundation while on leave from Purdue University, West Lafayette, IN, USA. Chiu is a Fellow of ASME and a Fellow of the Society for Imaging Science and Technology (IS&T) and an IEEE Senior Member.*

Jan P. Allebach *is Hewlett-Packard Distinguished Professor of Electrical and Computer Engineering at Purdue University. He is a Fellow of the National Academy of Inventors, IEEE, the Society for Imaging Science and Technology (IS&T), and SPIE. He was named the Electronic Imaging Scientist of the Year by IS&T and SPIE, and was named Honorary Member of IS&T, the highest award that IS&T bestows. He has received the IEEE Daniel E. Noble Award, the IS&T/OSA Edwin Land Medal, the IS&T Johann Gutenberg Prize, and is a member of the National Academy of Engineering.*